

Operando laser scattering: probing the evolution of local pH gradients on complex electrode architectures

Vitali Grozovski

University of Bern

Pavel Moreno-Garcia

University of Bern <https://orcid.org/0000-0002-6827-787X>

Elea Karst

University of Bern

María de Jesús Gálvez-Vázquez

University of Bern

Alexander Fluegel

BASF SE

Sathana Kitayaporn

BASF Corporation

Soma Vesztergom

Eötvös Loránd University <https://orcid.org/0000-0001-7052-4553>

Peter Broekmann (✉ peter.broekmann@dcb.unibe.ch)

University of Bern

Article

Keywords: pH gradients, Operando laser scattering

Posted Date: March 3rd, 2021

DOI: <https://doi.org/10.21203/rs.3.rs-257579/v1>

License: © ⓘ This work is licensed under a Creative Commons Attribution 4.0 International License.

[Read Full License](#)

Abstract

Self-assembly, complexation, agglomeration and precipitation phenomena relevant to biological, electrocatalytic and technological processes are strongly influenced by changes of the local pH at the solid-liquid interfaces where they occur. Understanding proton dynamics in the diffusion layers generated by these processes is of prime importance to improve their diagnosis and enable modelling and better control over them. Here we introduce a non-invasive pH-sensing approach that is based on the Tyndall effect enhancement modulated by pH-controlled agglomeration events. Using metal electrodeposition for advanced semiconductor wiring technology as a test vehicle, we demonstrate that our proposed strategy simultaneously provides real-time visualization of the pH dynamics and pH-guided reactivity with high spatial resolution without physically or chemically influencing the investigated surfaces. We suggest that its applicability can be universally extended to other relevant nanoaggregation/decomplexation processes occurring at light-addressable interfaces provided the probed colloids are smaller than the wavelength of visible light.

Introduction

Numerous redox reactions relevant to medical¹, biological², electrodeposition^{3,4}, corrosion⁵, electrocatalytic⁶, mineral recovery⁷ and electrocoagulation⁸ processes are of proton-coupled nature⁹, entailing localized pH changes as they proceed in aqueous media. This temporospatial variability of the proton concentration at electrified solid-liquid interfaces strongly influences and often dictates the kinetics of such processes as well as the near interface electrolyte speciation. Thus, knowledge of the proton diffusion dynamics in operating electrochemical setups under specific reaction conditions and in different aqueous environments allows to improve the understanding of the reaction mechanisms and enables optimized design and control of the processes. Therefore, several experimental approaches have been developed that address different aspects of local pH evolution at the micro and nanoscale. The most insightful and intensively used techniques to probe interfacial pH are based on fluorescence microscopy^{8,10}, scanning electrochemical microscopy (SECM)^{10,11}, vibrational spectroscopy^{4,12,13}, electrogenerated chemiluminescence¹⁴, micromesh-capped pH meters¹⁵ and rotating ring-disk electrodes (RRDEs)¹⁶. Another approach that enables access to the interfacial pH at molecular length scales and relies on the use of a concurrent non-faradaic pH-guided reaction was also recently reported¹⁷. Although all these analytical approaches have individually contributed to the understanding of interfacial pH dynamics, they are often limited by their spatial resolution, sensitivity and invasive nature and are typically restricted to simplified model systems¹⁸⁻²⁰. Thus, an integral *operando* method to probe surface pH in practical electrochemical setups that provides high spatial resolution without physically or chemically disturbing the investigated surface is still missing.

Herein we introduce a novel, inexpensive, rapid and non-invasive experimental strategy based on the Tyndall effect (TE) that enables long range real-time visualization of surface pH and pH-guided interfacial reactivity with high spatial resolution and sensitivity. Named after the physicist John Tyndall, TE is a type

of light scattering that takes place when visible light is passed through a colloidal solution with a particle size distribution that lies in the 400 to 750 nm range²¹. This phenomenon has already been used as a visual screening method to detect microprecipitates in blends of parental drug solutions^{22,23} as well as to evaluate nanolevel aggregation and characterise colloidal catalyst and functional materials²⁴⁻²⁷. More recently, Xiao et al.²⁸ added quantitative character to a TE-based colorimetry approach and demonstrated a *ca.* 1000-fold sensitivity improvement compared to common surface plasmon resonance-based techniques. In this work we bring forward this approach and demonstrate its excellent capabilities to investigate proton dynamics at electrified solid-liquid interfaces using a technologically relevant process as a test vehicle, namely superconformal Co electrodeposition (CoED) for advanced semiconductor wiring technology. Specifically, we investigate superconformal CoED on actual patterned Si wafers under *quasi* practical process conditions. Note that assessment of surface pH in these systems is very challenging as the employed Si wafers bear distinct recessed patterned fields along their surface and present, therefore, heterogeneous spatial reactivities for competitive proton and metal ion reduction. To enable the spatiotemporal visualization of pH gradients and pH-guided reactivity, we exploited an intrinsic recognition event of superconformal CoED that leads to complexation of a pH-sensitive compound with Co^{2+} ions at a critical local pH value that develops as the deposition proceeds. This pH-controlled aggregation results in substantial enhancement of the TE read-out observed via a laser beam positioned immediately adjacent to the sample surface and recorded with an ordinary camera.

Results And Discussion

Superconformal CoED on patterned Si wafers

Until recently, the manufacture of microprocessor wiring has almost exclusively been based on superconformal Cu electrodeposition (CuED) processes on patterned Si wafers²⁹. However, the critical dimension of current microchip structures has nowadays approached the electron mean free path (MFP) of copper, introducing new challenges to the continuous scaling of interconnects for the 7 nm technology node and beyond³⁰⁻³². In this context, Co is thought to be less prone to resistance scaling effects and therefore more suitable for further downsizing device dimensions³³⁻³⁵. Figure 1a shows a micrograph of a 300 mm Si wafer containing hundreds of advanced processor dies whose components are interconnected by void-free electrodeposited Co and Cu wiring. The specimen displayed by Fig. 1b reveals the intricate architecture of individual dies before metal deposition that comprise micro and nanoscale circuitry. Note that the manufacture of the novel Co interconnects by wet methods poses new technological challenges³⁶.

Figure 1c schematically summarizes the electrochemical components of the overall surface process occurring during superconformal Co electroplating of patterned Si wafers. Specifically, unlike CuED, CoED processes carried out from aqueous plating baths are unavoidably accompanied by the hydrogen evolution reaction (HER), thereby developing pH gradients adjacent to the surface of the patterned wafers as they proceed³⁷⁻³⁹. The reaction rate of these two components (CoED and HER) is expressed in Fig. 1c

in terms of their respective position-dependent electric current densities j_{Co} and j_{HER} . The scheme illustrates the strong dependence of the effective Co deposition (j_{Co}) and the parasitic HER (j_{HER}) on the specific local topography of the substrate. Thus, bottom-up metal deposition and H₂ evolution occur preferentially on the recessed patterned features and their inhibition takes place on the non-patterned/planar surface regions. This enables the so-called superconformal CoED on high aspect ratio patterned features that is schematically shown in the inset of Fig. 1c. These differential Co deposition and H₂ evolution are achieved by the action of an inhibitor additive that is selectively adsorbed on the planar areas and upper side walls of the patterned trenches^{36, 40}. Moreover, an electrochemically inactive but pH-sensitive compound is employed to probe the evolution of local pH gradients across the interface. The delayed activation of this compound is indeed achieved through its pH-guided aggregation.

pH-triggered aggregation of the pH-probe

Supplementary Fig. 1 presents beaker-scale TE experiments in which a green laser beam (532 ± 10 nm, 5 mW, beam diam. 2.5 mm) is passed through a series of inhibitor- and pH-probe-containing Co plating baths (50 mM CoSO₄ in 0.5 M H₃BO₃) with different pH values ranging from 2 to 6. Control experiments carried out with plating solutions containing no pH-sensing compound are also shown. These results demonstrate that TE enhancement by aggregation phenomena occur when the solution pH surpasses the value of 4.5 only in the plating bath that contains the pH-sensing compound. This aggregation stems from deprotonation of the pH-probe compound at that critical pH 4.5 followed by complexation with the Co²⁺ ions present in the electrolyte, thus leading to local precipitation of cross-linked agglomerates. The presence of Co²⁺ species in those precipitates was revealed by elementary EDX analysis in combination with control beaker scale TE experiments (Supplementary Figs. 2 and 3).

As above mentioned, when conducting additive-assisted metallization of the patterned wafers both CoED and HER preferentially take place on the recessed areas. Under typically applied process conditions, as the Co deposition proceeds on the recessed areas, a local pH gradient appears and develops at the front of the rising metal growth owing to H⁺ consumption and mass transport limitations. Fig. 2a-b illustrates the corresponding dynamics of the interfacial double layer. In a further stage of the process the synchronized consumption of H⁺ ions on top of the trenches (with pH reaching the critical value) and completion of superconformal metal filling results in pH-probe precipitation in front of the filled patterned areas.

Colorimetry approach based on TE enhancement at electrified patterned Si dies

In the following we show how we exploit these pH-driven surface agglomeration phenomena to address visualization of local proton dynamics in real time at the microscopic level over extended electrode areas with high spatial resolution. Fig. 3a illustrates the operating principle of the developed *operando* TE-based colorimetry approach. The galvanostatic Co plating experiments (*i.e.*, at constant j) were carried out on single patterned Si dies in an electrochemical glass cell with plating electrolytes (50 mM Co₂SO₄ in

0.5 M H_3BO_3) containing the inhibitor- and pH-sensing compound. The electrolytes with initial pH 2.5³⁶ were agitated at different frequencies by a magnetic stirrer at 100-300 rpm to mimic solution flow on the die surface similar to the solution flow applied in a real plating tool. A large surface area Pt wire acted as anode and the measurements were controlled by an Autolab 302N potentiostat/galvanostat Metrohm system. Two non-invasive optical probes consisting of two green laser beams operated at equal intensities, aligned in parallel and separated by 5 mm from each other were accurately positioned by a differential micrometer screw so that they passed just adjacent to the outermost sample surface during the Co electroplating experiments. The primary laser probe (L1) was passed over rows of patterned fields bearing features with varying feature pitch (40-120 nm) and 100 nm average trench depth while the secondary laser beam (L2) probed the surface of non-patterned mirror-like sample locations (Fig. 3b). A conventional camera outside the glass cell positioned in front of the sample surface as depicted in Fig. 3c was used to record the time-evolution of the TE enhancement and the associated pH dynamics.

Real-time visualization of pH dynamics and CoED process progression

The time evolution of surface pH and agglomeration events enabled by the proposed approach are exemplarily illustrated in Fig. 4. The micrograph presented in Fig. 4a shows the geometry and characteristic dimensions of the patterned domains that were monitored by the laser L1. Fig. 4b displays selected screenshots recorded by the camera at progressive stages during Co deposition. Additional experiments at 100 rpm applied solution stirring are provided by Supplementary Fig. 4 and the corresponding video. The labels on the upper left corner in each subpanel indicate the time elapsed (t) after the electrochemical process was initiated. The absence of TE enhancement on the die surface indicates that the surface pH remains lower than 4.5 during the first six seconds of electrodeposition at all sample locations. Then at $t = 7$ s light scattering events start becoming apparent only at specific sample locations adjacent to the probing laser L1 (only on patterned sample regions with feature pitch 40-50 nm that develop large local current densities). Conversely, no apparent scattering events other than background events can be observed at the interfacial sample regions probed by L2. This indicates that at this stage, precipitation of the pH-probe compound selectively takes place at those patterned sample locations because their local pH reaches the critical value due to HER as the front of the deposited Co approaches the outermost sample surface. Note that these agglomeration events remain physically confined to the parallel patterned domains that in the probed surface region are separated from each other by 50 mm spacings (see Supplementary Fig. 5) and that fields with larger feature pitch (85-120 nm) where the local current density is comparably lower have not yet reached the critical pH. This proves that our approach enables 3D mm-scale spatial resolution of the local pH-guided reactivity over laterally extended macroscopic samples and that the intensity of the associated TE enhancement directly correlates with the position dependent current density.

As the electrodeposition proceeds, within $8 \text{ s} \leq t \leq 15 \text{ s}$, an increasing number of patterned fields gradually achieve successful superconformal filling and the concomitant change of pH and pH-probe precipitation occurring in the locations probed by L1 can be instantly and straightforwardly followed based on the observed scattering enhancement. At $t = 16$ s the increase in pH far beyond the critical value

and the accumulation of precipitated Co^{2+} -pH-probe complex become obvious from the increased TE enhancement at those locations that were firstly filled. At this moment light scattering becomes observable for the first time on the non-patterned sample surface probed by the L2 beam. The reason for this delay in local pH increase and accompanying pH-probe precipitation is the presence of the inhibitor layer adsorbed on the flat sample areas that slows down the kinetics of both the HER and CoED³⁶. Continuation of the galvanostatic Co deposition eventually leads to the interfacial pH surpassing the marker threshold at all sample locations that results in the even Co deposition along the entire Si die. Specifically, at $t \geq 24$ s the increased $\text{pH} > 4.5$ on top of the flat sample locations separating recessed domains leads to losses in spatial resolution. Finally, at $t \geq 35$ s massive Co^{2+} -pH-probe precipitation due to the progressive alkalisation of the diffusion layer all over the sample sets in and both L1 and L2 probes reveal increasingly similar scattering phenomena. The higher intensity of the light scattering is, nonetheless, still observable on the patterned regions.

To demonstrate that the observed pH dynamics and resulting agglomeration originate from surface-confined electrochemically-driven transformations we carried out the following control investigations. First, CoED experiments performed under identical plating conditions as discussed above but placing the laser system 50 mm away from the sample surface exhibited much weaker scattering enhancement. Further, a second series of reference experiments carried out with laser irradiation adjacent to the sample surface but without pH-probe in the plating electrolyte showed no TE enhancement at all surface metallization stages. Finally, experiments with all plating components but conducted at zero total transferred charge (in the absence of electrochemical processes) equally showed no TE enhancement. The corresponding supplementary Figs. 6-8 are included in the Supplementary Information file.

Confirmation by numerical simulations

The scenario described before can also be confirmed by finite element-based numerical simulations if we assume variables (Co^{2+} concentration, pH , applied current density j) that exactly match the applied experimental conditions, and we use physical parameter values (charge transfer and reaction rate coefficients) in the simulations that were described elsewhere for Co electrodeposition. In the simulation routine (details are explained in the Supplementary Information file), it is enough to handle two simultaneously occurring electrode processes (CoED and the HER) and to account for mass transfer processes supplying reactants. To deal with surface heterogeneities, we assumed that both electrode reactions have a 100-fold decreased activity over the (additive-blocked) planar surfaces, while the reactions run unhindered at trenched areas. Fig. 5 presents the time evolution of pH profiles on the surface of a simulated Si die segment that comprises three patterned fields (black recessed rectangles). Selected screenshots of the proton dynamics at times matching those displayed in Fig. 4b are shown and those of the corresponding Co^{2+} concentration profiles can be found in supplementary Fig. 9. Both pH and Co^{2+} concentration profiles show that protons and Co^{2+} ions are more rapidly consumed on the surface of the patterned fields than on flat sample areas in the course of the plating process. Note in Fig. 5 that as the electrolysis proceeds, the resulting accelerated alkalisation beyond the critical pH value at

$t = 9$ s initially remains confined on top of the recessed fields and that for the following 3 s there is no overlap of individually developing mushroom-like pH profiles. This matches the evolution of the pH-guided precipitation phenomena revealed by the L1 probe during the first 16 s in Fig. 4b. Despite the slight temporal mismatch between the experimental and the simulated data, their qualitative agreement with regards to pH dynamics and pH-guided agglomeration is remarkable. At more advanced process stages ($t > 12$ s in Fig. 5), attainment and subsequent surpassing of the critical pH value not only on recessed areas but also on top of the adjacent flat sample locations leads to the loss in lateral spatial resolution of the interfacial pH concomitant with the expansion of the diffusion layer. This correlates with the experimental Tyndall effect observations at $t \geq 24$ s in Fig. 4b.

Overall, the presented *operando* TE-based approach constitutes a significant progress in analytical strategies aiming at investigating the dynamics of the interfacial double layer because it provides instantaneous extended pH read-out on surfaces with distinct local reactivities and unique spatiotemporal resolution only limited by the acquisition capabilities of the employed camera (here 30 three-dimensional reactivity maps per second). Besides straightforwardly enabling comparative reaction kinetics intrinsic to complex electrode architectures, the approach is also amenable to quantification and exhibits outstanding sensitivity²⁸. Finally, its applicability can be universally extended to any other nanoaggregation/decomplexation process of interest (*e.g.*, electrocoagulation, mineral removal and separation, electrosynthesis, among others) occurring at light-addressable interfaces provided the probed colloids are smaller than the wavelength of visible light. This work provides therefore useful means to improve the understanding of such interfacial processes and control over them.

Methods

Chemicals, plating solution and electrochemical cell. $\text{CoSO}_4 \cdot 7\text{H}_2\text{O}$ (ReagentPlus, 99%) and H_3BO_3 (trace metal basis, 99.97%) were purchased from Sigma-Aldrich. H_2SO_4 (96% Suprapure) was purchased from Merck. The solution for cobalt plating (50 mM $\text{CoSO}_4 \cdot 7\text{H}_2\text{O}$, 0.5 M H_3BO_3) was prepared from as-received chemicals and deionized water (18.2 M Ω cm, TOC 3 ppb, Millipore). The plating bath's pH was set by addition of H_2SO_4 and monitoring with a calibrated pH/conductometer (Metrohm 914, The Netherlands). The native pH-probe with pKa 4.5 value also served as a marker for the local pH measurements. All electrochemical measurements were performed at room temperature by a potentiostat/galvanostat system (Metrohm Autolab 302N, The Netherlands) in a three electrode configuration using a custom made glass cell (total solution volume of 200ml). A double junction Ag/AgCl_{3M} electrode (Metrohm, Switzerland) and a large surface area Pt wire (99.99% MaTeck) were used as reference and counter electrodes, respectively. The working electrodes for Co deposition were Co-seeded patterned wafer coupons and Co-seeded blanket wafers (40nm seed) for selected control experiments. The feature pitch of the patterned areas used had a pitch from 40 to 1000 nm and an average trench depth of 100 nm. Every single patterned field had dimensions of 1 x 0.265 mm² and was arranged into stacks as shown in Fig. 4a. 2D non-patterned sample regions with mirror-like finish were studied for comparison. A single wafer coupon was used for each deposition experiment to provide identical initial conditions across all

experiments. The recorded electrochemical data was logged in Nova 2.1 software (Metrohm, The Netherlands).

Laser setup. The optical probe in this study consists of two parallel 5mW green lasers (532 ± 10 nm) operated with DC power supply (RND Lab) at fixed potential and current settings (2.88 V and 0.3 A) that provided equal light intensities. The laser beams were collimated and exhibited a cross section of 2.5 mm in diameter. Accurate laser alignment and positioning adjacent to patterned stacks and non-patterned areas were achieved through a manual ProbeHead (PH120, Süss Microtek) and a differential micrometre screw (Thorlabs).

Video capture. All images and videos presented in the main text and supplementary information file were recorded with a Canon 600D digital single lens reflex camera with video capabilities. A Canon lens (EF 100mm f2.8 Macro USM) was used together with a teleconverter (Tokina 1.4x Teleplus Pro 300) that provided a final aperture of f4.0 and a focal length of 224 mm in 35 mm equivalent format. The videos were recorded at fixed exposure settings 1/30s and f5.6, iso800. The frame acquisition rate was set to 30 s^{-1} . Besides the minor ambient lab illumination (fluorescent light), no additional light sources were present in the lab. No white balance or any other exposure compensation/tuning was used during filming. The camera was supported on a tripod via a lens supporting collar. The raw video data was processed using the OpenShot Video Editor on a Ubuntu 18.04 Linux workstation with further frame by frame development and cutting single images in VLC Media player software.

Procedure to record TE enhancement during CoED. Galvanostatic Co deposition was performed at $j = -1 \text{ mA cm}^{-2}$ on the basis of the geometric wafer surface area left exposed to the electrolyte. A “cold entry” sample immersion procedure was implemented with the following step sequence: i) die immersion at open circuit potential (OCP) into the additive-containing plating bath (50 mM CoSO_4 in 0.5 M H_3BO_3), ii) adjustment of laser position relative to the Si die, iii) initiation of video recording, iv) application of the constant current density for additive CoED. The positions of L1 and L2 probing beams were first adjusted using a dummy sample to avoid Co seed dissolution from the patterned wafer. Once the desired positioning and laser alignment were attained, the dummy sample was removed and replaced by the actual patterned wafer to be metalized. The solution was agitated throughout the deposition process using a 15 mm x 6 mm magnetic stirrer bar operating at 100 or 300 rpm to mimic solution flow at the wafer surface similar to the solution flow in a real plating tool. Two to four repetitions per plating parameter set were performed to confirm experimental reproducibility.

Reference measurements by means of a conventional pH probe. Reference local pH measurements recorded with an invasive probe were performed with a calibrated pH micro electrode (Orion) coupled to the potentiostat/galvanostat instrument via a pX1000 module (Metrohm, The Netherlands). The pH micro probe (diam = 1 mm) was supported and moved by the differential micrometre screw for precise and fine positioning. The maximal separation between the pH micro probe and the wafer surface was determined with an optical close-up tube (Macroscope 25 8x30 Monocular, RF Inter-Science Co, NY) and did not exceed 50 μm . These pH reference measurements were performed with the same set of deposition

parameters applied in the TE-based approach. The probe was positioned at the closest possible position to the wafer surface (patterned and non-patterned areas). The corresponding electrical current was applied and the time evolution of pH was recorded. The probe output (voltage and pH) was logged in the Nova 2.1 software along with the time and applied current/potential values. After having finished the Co deposition the wafer was inspected by SEM and optical microscopy to reveal possible shielding effects by the invasive probe. It was found that the pH micro probe was not sensitive enough to accurately follow the time evolution of the surface pH developed upon CoED. Moreover, the successful superconformal metallization of the features adjacent to the pH probe was not achieved owing to interference with the natural diffusion of electrolyte species and possible distortion of the electric field.

Declarations

Acknowledgements

P.B. acknowledges financial support from the Swiss National Foundation (grant 200020–172507). S.V. acknowledges support from the National Research, Development and Innovation Office of Hungary (NKFIH grants FK135375).

Author contributions

These authors contributed equally: Vitali Grozovski, Pavel Moreno-García.

P.B. supervised the project. V.G. designed and performed the experiments. E.K. performed the experiments. M.d.J.G.V. performed the experiments. S.V. carried out the theoretical simulations. P.M.G. and V.G. analysed and discussed the data. P.M.G., V.G., S.V., P. B., A.F. and S.K. prepared and wrote the manuscript.

Competing interests

The authors declare no competing interest.

Additional information

Supplementary information is available for this paper at

Correspondence and requests for materials should be addressed to P.M.G. and P.B.

References

1. Düwel, S. et al. Imaging of pH in vivo using hyperpolarized ^{13}C -labelled zymonic acid. *Nat. Commun.* **8**, 15126 (2017).
2. Joshi, V.S., Sheet, P.S., Cullin, N., Kreth, J. & Koley, D. Real-Time Metabolic Interactions between Two Bacterial Species Using a Carbon-Based pH Microsensor as a Scanning Electrochemical Microscopy Probe. *Anal. Chem.* **89**, 11044-11052 (2017).

3. Salles, R.C.M., de Oliveira, G.C.G., Díaz, S.L., Barcia, O.E. & Mattos, O.R. Electrodeposition of Zn in acid sulphate solutions: pH effects. *Electrochim. Acta* **56**, 7931-7939 (2011).
4. Homma, T., Kunimoto, M., Sasaki, M., Hanai, T. & Yanagisawa, M. Surface enhanced Raman spectroscopy measurement of surface pH at the electrode during Ni electrodeposition reaction. *J. Appl. Electrochem.* **48**, 561-567 (2018).
5. Filotás, D. et al. Improved potentiometric SECM imaging of galvanic corrosion reactions. *Corros. Sci.* **129**, 136-145 (2017).
6. Koper, M.T.M. Theory of multiple proton–electron transfer reactions and its implications for electrocatalysis. *Chem. Sci.* **4**, 2710-2723 (2013).
7. Lei, Y., Song, B., van der Weijden, R.D., Saakes, M. & Buisman, C.J.N. Electrochemical Induced Calcium Phosphate Precipitation: Importance of Local pH. *Environ. Sci. Technol.* **51**, 11156-11164 (2017).
8. Fuladpanjeh-Hojaghan, B. et al. In-Operando Mapping of pH Distribution in Electrochemical Processes. *Angew. Chem. Int. Ed.* **58**, 16815-16819 (2019).
9. Costentin, C., Robert, M. & Savéant, J.-M. Update 1 of: Electrochemical Approach to the Mechanistic Study of Proton-Coupled Electron Transfer. *Chem. Rev.* **110**, PR1-PR40 (2010).
10. Boldt, F.-M., Heinze, J., Diez, M., Petersen, J. & Börsch, M. Real-Time pH Microscopy down to the Molecular Level by Combined Scanning Electrochemical Microscopy/Single-Molecule Fluorescence Spectroscopy. *Anal. Chem.* **76**, 3473-3481 (2004).
11. Monteiro, M.C.O., Jacobse, L., Touzalin, T. & Koper, M.T.M. Mediator-Free SECM for Probing the Diffusion Layer pH with Functionalized Gold Ultramicroelectrodes. *Anal. Chem.* **92**, 2237-2243 (2020).
12. Zakaria, S.N.A. et al. Insight into the Nature of Iron Sulfide Surfaces During the Electrochemical Hydrogen Evolution and CO₂ Reduction Reactions. *ACS Appl. Mater. Interfaces* **10**, 32078-32085 (2018).
13. Yang, K., Kas, R. & Smith, W.A. In Situ Infrared Spectroscopy Reveals Persistent Alkalinity near Electrode Surfaces during CO₂ Electroreduction. *J. Am. Chem. Soc.* **141**, 15891-15900 (2019).
14. Jirka, G.P., Martin, A.F. & Nieman, T.A. pH and concentration response surfaces for the luminol–H₂O₂ electrogenerated chemiluminescence reaction. *Anal. Chim. Acta* **284**, 345-349 (1993).
15. Deligianni, H. & Romankiw, L.T. In situ surface pH measurement during electrolysis using a rotating pH electrode. *IBM J. Res. Dev.* **37**, 11 (1993).
16. Zimer, A.M. et al. Development of a versatile rotating ring-disc electrode for in situ pH measurements. *Anal. Chim. Acta* **897**, 17-23 (2015).
17. Ryu, J., Wuttig, A. & Surendranath, Y. Quantification of Interfacial pH Variation at Molecular Length Scales Using a Concurrent Non-Faradaic Reaction. *Angew. Chem. Int. Ed.* **57**, 9300-9304 (2018).
18. Critelli, R.A.J., Bertotti, M. & Torresi, R.M. Probe effects on concentration profiles in the diffusion layer: Computational modeling and near-surface pH measurements using microelectrodes. *Electrochim.*

- Acta* **292**, 511-521 (2018).
19. Leenheer, A.J. & Atwater, H.A. Imaging Water-Splitting Electrocatalysts with pH-Sensing Confocal Fluorescence Microscopy. *J. Electrochem. Soc.* **159**, H752-H757 (2012).
 20. Ji, J., Cooper, W.C., Dreisinger, D.B. & Peters, E. Surface pH measurements during nickel electrodeposition. *J. Appl. Electrochem.* **25**, 642-650 (1995).
 21. Gentry, J.W. The legacy of John Tyndall in aerosol science. *J. Aerosol Sci.* **28**, 1365-1372 (1997).
 22. Veggeland, T. & Brandl, M. Evaluation of a Simple Method for Visual Detection of Microprecipitates in Blends of Parenteral Drug Solutions Using a Focussed (Tyndall) Light Beam. *Int. J. Pharm. Compd.* **14**, 4 (2010).
 23. Staven, V., Waaseth, M., Wang, S., Grønlie, I. & Tho, I. Utilization of the Tyndall Effect for Enhanced Visual Detection of Particles in Compatibility Testing of Intravenous Fluids: Validity and Reliability. *PDA J. Pharm. Sci. and Tech.* **69**, 270-283 (2015).
 24. Cheng, Y., Ou, X., Ma, J., Sun, L. & Ma, Z.-H. A New Amphiphilic Brønsted Acid as Catalyst for the Friedel–Crafts Reactions of Indoles in Water. *Eur. J. Org. Chem.* **2019**, 66-72 (2019).
 25. Raizada, P. et al. Fabrication of Ag₃VO₄ decorated phosphorus and sulphur co-doped graphitic carbon nitride as a high-dispersed photocatalyst for phenol mineralization and E. coli disinfection. *Sep. Purif. Technol.* **212**, 887-900 (2019).
 26. Lei, W. et al. Boron nitride colloidal solutions, ultralight aerogels and freestanding membranes through one-step exfoliation and functionalization. *Nat. Commun.* **6**, 8849 (2015).
 27. Cui, J., Kim, G., Kim, S., Kwon, J.E. & Park, S.Y. Ultra-pH-Sensitive Small Molecule Probe Showing a Ratiometric Fluorescence Color Change. *ChemPhotoChem* **4**, 393-397 (2020).
 28. Xiao, W. et al. Highly Sensitive Colorimetric Detection of a Variety of Analytes via the Tyndall Effect. *Anal. Chem.* **91**, 15114-15122 (2019).
 29. Andricacos, P.C. Copper On-Chip Interconnections A Breakthrough in Electrodeposition to Make Better Chips. *Interface* **8**, 32-37 (1999).
 30. Josell, D., Brongersma, S.H. & Tókei, Z. Size-Dependent Resistivity in Nanoscale Interconnects. *Annual Review of Materials Research* **39**, 231-254 (2009).
 31. Barmak, K. et al. Surface and grain boundary scattering in nanometric Cu thin films: A quantitative analysis including twin boundaries. *Journal of Vacuum Science & Technology A* **32**, 061503 (2014).
 32. Huang, Q., Lyons, T.W. & Sides, W.D. Electrodeposition of Cobalt for Interconnect Application: Effect of Dimethylglyoxime. *J. Electrochem. Soc.* **163**, D715-D721 (2016).
 33. Gall, D. Electron mean free path in elemental metals. *Journal of Applied Physics* **119**, 085101 (2016).
 34. Sankaran, K., Clima, S., Mees, M. & Pourtois, G. Exploring Alternative Metals to Cu and W for Interconnects Applications Using Automated First-Principles Simulations. *ECS J. Solid State Sci. Technol* **4**, N3127-N3133 (2014).
 35. Lee, C.H., Bonevich, J.E., Davies, J.E. & Moffat, T.P. Superconformal Electrodeposition of Co and Co–Fe Alloys Using 2-Mercapto-5-benzimidazolesulfonic Acid. *J. Electrochem. Soc.* **156**, D301 (2009).

36. Moreno-García, P. et al. Inverted RDE (iRDE) as Novel Test Bed for Studies on Additive-Assisted Metal Deposition under Gas-Evolution Conditions. *J. Electrochem. Soc.* **167**, 042503 (2020).
37. Kongstein, O.E., Haarberg, G.M. & Thonstad, J. Mass Transfer of Protons during Electrodeposition of Cobalt in Chloride Electrolytes. *J. Electrochem. Soc.* **157**, D335 (2010).
38. Rigsby, M.A. et al. The Critical Role of pH Gradient Formation in Driving Superconformal Cobalt Deposition. *J. Electrochem. Soc.* **166**, D3167-D3174 (2018).
39. Kongstein, O.E., Haarberg, G.M. & Thonstad, J. Current efficiency and kinetics of cobalt electrodeposition in acid chloride solutions. Part I: The influence of current density, pH and temperature. *J. Appl. Electrochem.* **37**, 669-674 (2007).
40. Wu, J., Wafula, F., Branagan, S., Suzuki, H. & van Eisdien, J. Mechanism of Cobalt Bottom-Up Filling for Advanced Node Interconnect Metallization. *J. Electrochem. Soc.* **166**, D3136-D3141 (2018).

Figures

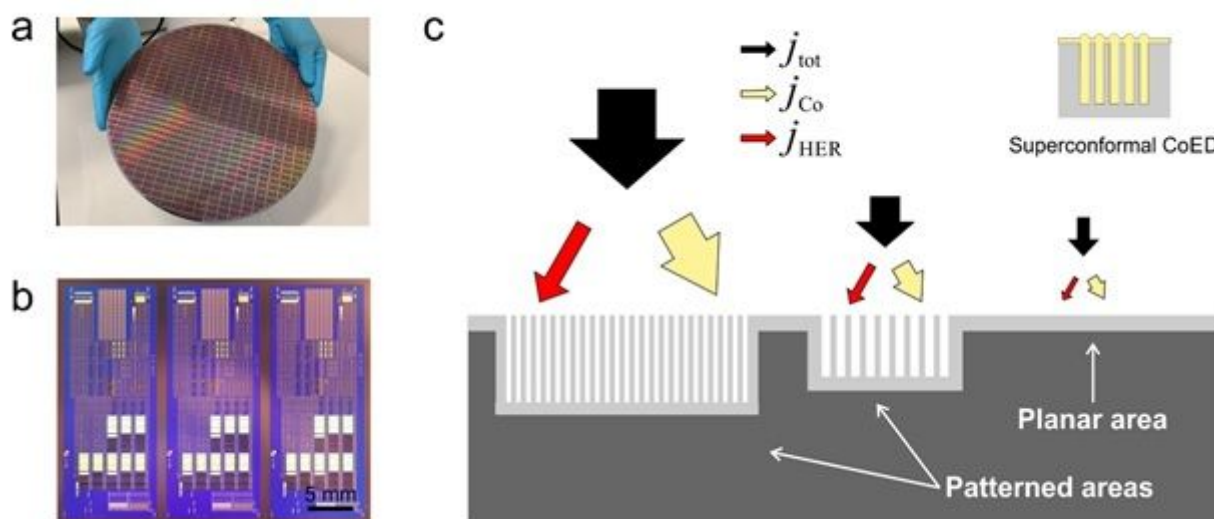


Figure 1

CoED processes for cutting-edge interconnect technology. (a) A 300 mm Si wafer bearing hundreds of processor dies manufactured by lithographic and electrochemical deposition methods (CoED and CuED). (b) Magnified view of a 300 mm Si wafer before Co metallization that reveals the internal structural complexity of individual patterned dies. (c) Schematic representation of the position-dependent current density distribution along the surface of a patterned wafer during CoED. j_{Co} and j_{HER} stand for the partial current density contributions to the total current density j_{tot} from CoED and parasitic HER, respectively. The inset in (c) schematically shows cross-sectioned trenches after having been superconformally electroplated.

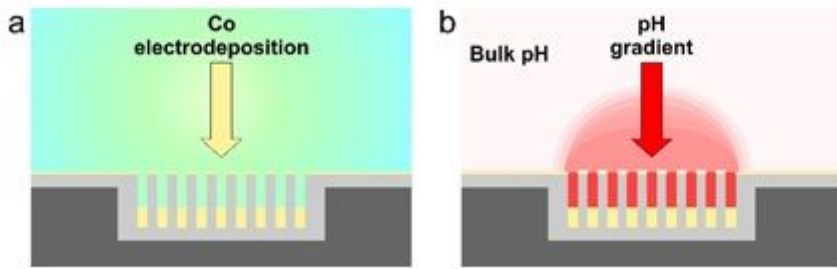


Figure 2

Evolution of the interfacial double layer that develops during Si wafer metallization by superconformal CoED. (a) and (b) Dynamics of the metal deposition and proton reduction taking place in the course of CoED on patterned wafers.

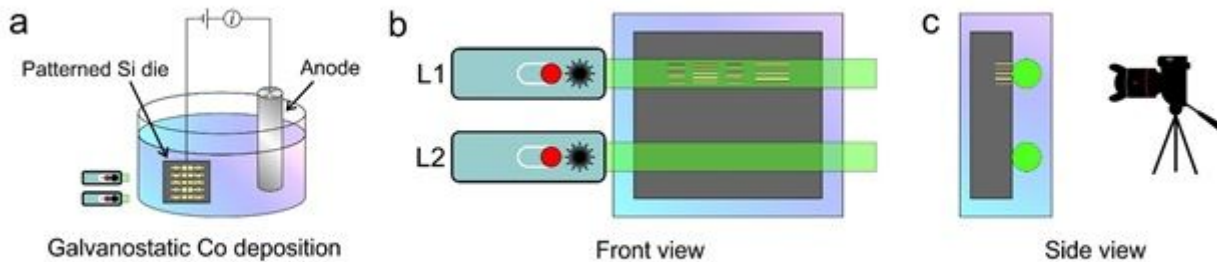


Figure 3

Schematic representation of the operando TE-based colorimetry approach for assessment of pH and agglomeration dynamics at electrified Si dies. (a) Experimental arrangement for CoED experiments coupled to pH probing by a non-invasive tandem laser beam. (b) and (c) Front and side views of the laser probe positioning relative to the Si die during sample metallization.

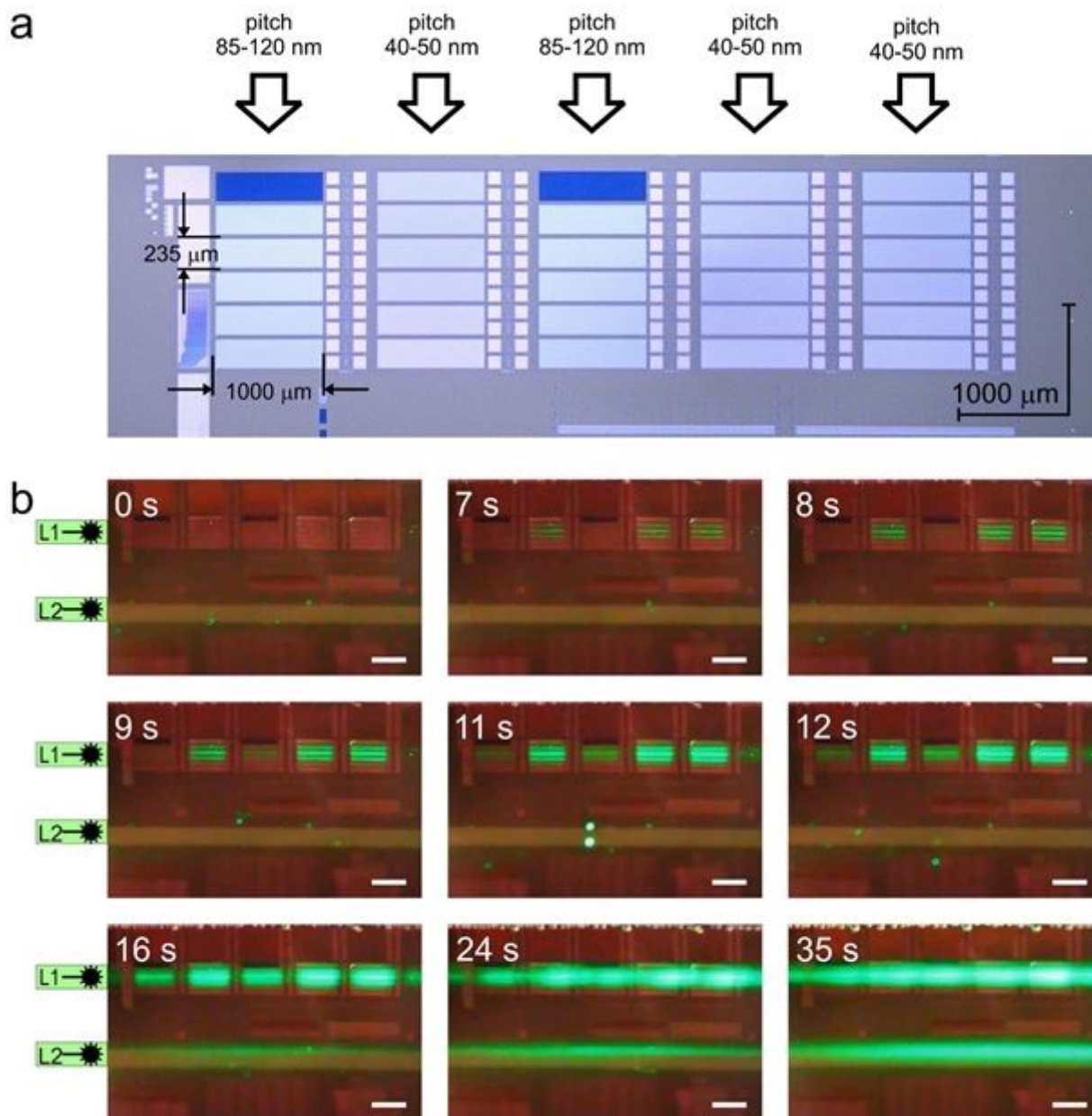


Figure 4

Time-evolution of TE enhancement on the surface of a patterned Si die during superconformal galvanostatic CoED experiments. (a) Optical micrograph of a Co-seeded Si die section scrutinized by the TE-based colorimetry approach. The characteristic feature pitch of each patterned ensemble is indicated by arrows. (b) Selected screenshots captured at different stages of the superconformal Co electrodeposition process by a camera placed in front of the Si die. The labels on the upper left corner of each subpanel indicate the time elapsed after the galvanostatic metal deposition was started. Scale bars: 1000 μm for all subpanels in (b). The plating bath contained both inhibitor additive and pH-sensitive compound and the CoED was conducted at $j = -1 \text{ mA cm}^{-2}$ and 300 rpm. Each adjacent patterned

domain probed by L1 comprises an area of 0.265 mm² and is separated from the closest neighbours by 50 μ m.

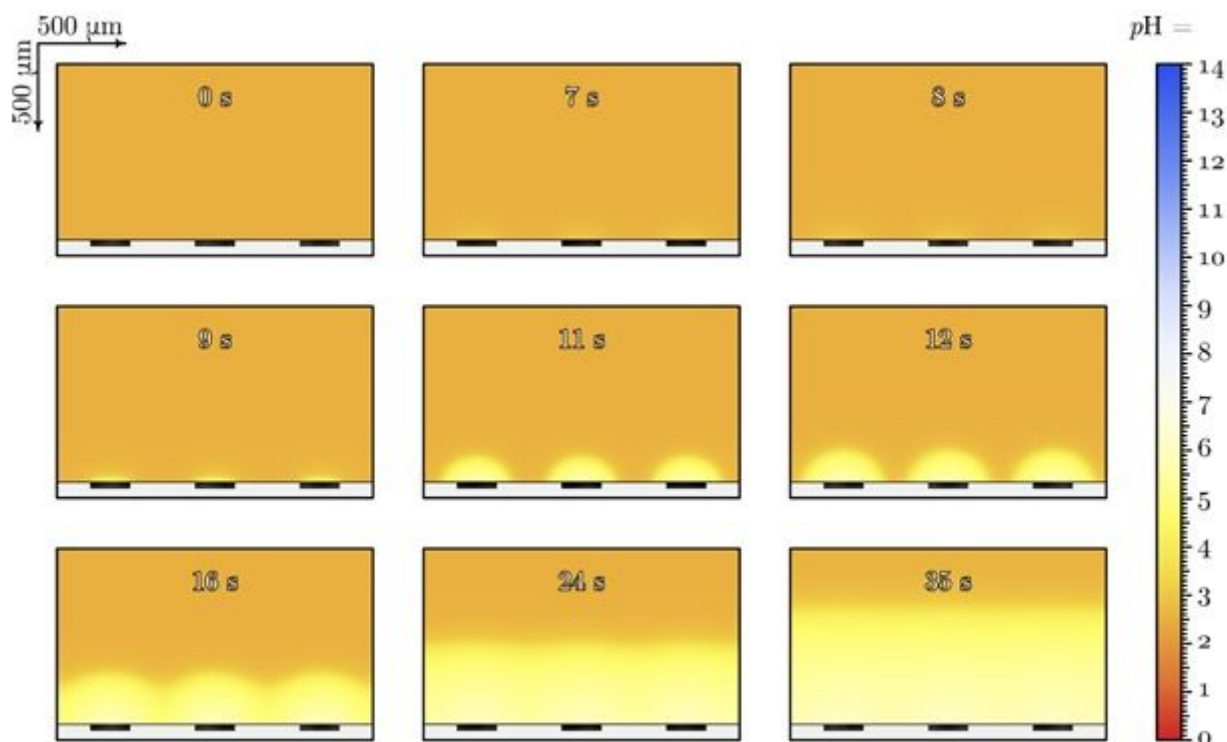


Figure 5

Simulated pH profiles on a Si die segment comprising three patterned fields. Selected screenshots of pH profiles captured at different stages of the simulated Co electrodeposition process. The labels on the upper central part of each subpanel indicate the time elapsed after the galvanostatic metal deposition at $j = -1 \text{ mA cm}^{-2}$ had been started. The initial pH of the plating bath at $t = 0$ was set to 2.5. The blocking effect of the inhibitor additive adsorbed on non-patterned sample surface regions is achieved in the calculations by setting $k_{\text{HER}}(\text{flat})/k_{\text{HER}}(\text{patterned}) = 100$, where k_{HER} stands for the reaction rate coefficient for the HER.

Supplementary Files

This is a list of supplementary files associated with this preprint. Click to download.

- [SupplementaryInformation.docx](#)
- [FigureS4video.mp4](#)
- [FigureS6video.mp4](#)
- [FigureS7video.mp4](#)

- [FigureS8video.mp4](#)